Fracture Characteristics of Monolayer

CVD-Graphene

Yun Hwangbo,[1, #] Choong-Kwang Lee,[2, #] Sang-Min Kim,[1] Jae-Hyun Kim,[1,3] Kwang-Seop Kim,[1] Bongkyun Jang,[1] Hak-Joo Lee,[1] Seoung-Ki Lee,[4] Seong-Su Kim,[2] Jong-Hyun Ahn, [4,] * and Seung-Mo Lee[1,3] *

[1] Department of Nanomechanics, Nano-Convergence Mechanical Systems Research Division, Korea Institute of Machinery & Materials (KIMM), 156 Gajungbuk-ro, Yuseong-gu, Daejeon, 305-343, South Korea

[2] Department of Organic Materials & Fiber Engineering, Chonbuk National University, Jeonju, 561-756, South Korea

[3] Nano Mechatronics, University of Science and Technology (UST), 217 Gajeong-ro, Yuseong-gu, Daejeon 305-333, South Korea

[4] School of Electrical and Electronic Engineering, Yonsei University, Seoul, 120-749, South Korea

[#] These authors contribute equally.

*Corresponding Authors: Prof. Dr. Seung-Mo Lee (sm.lee@kimm.re.kr), Prof. Dr. Jong-Hyun Ahn (ahnj@yonsei.ac.kr)

Included:
- **1. Supplementary Figures (Figure S1-S17)**
- **2. Supplementary Tables (Table S1-S4)**
- **3.-6. Supplementary Discussion I, II, III, IV**
- **7. Supplementary 4 Movies (Movie S1- S4)**
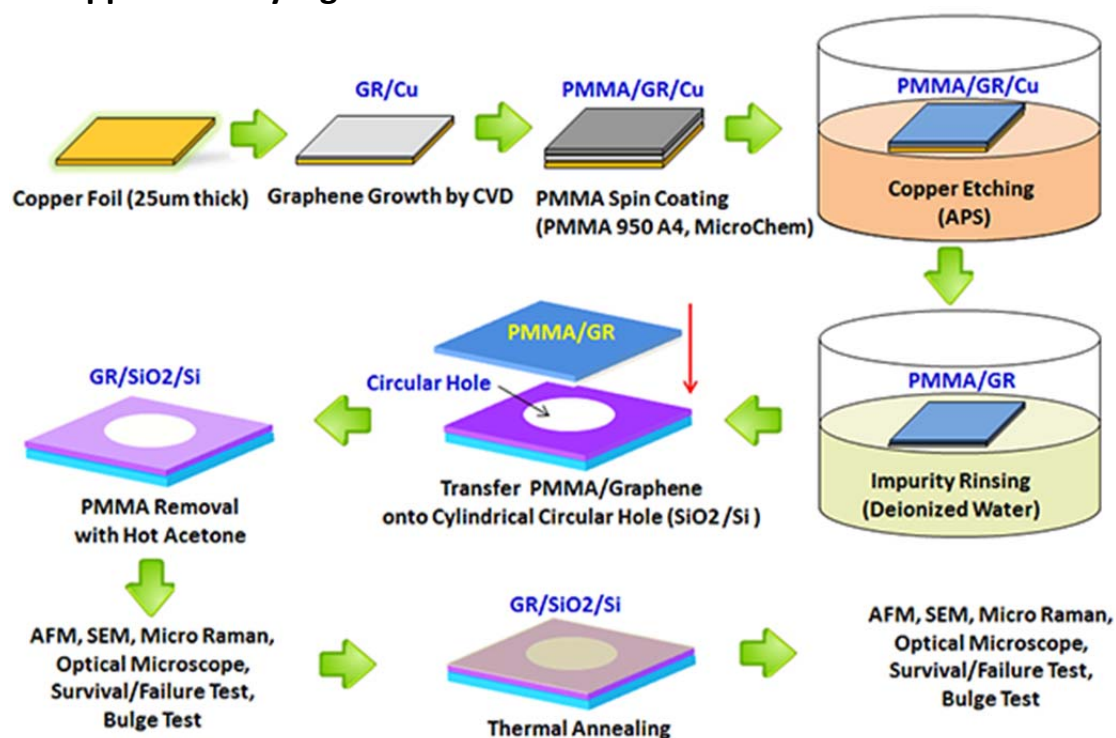- **8. Supplementary References**

1. Supplementary Figures

Figure S1. Preparation procedures of the suspended membrane from CVD-graphene on the Si substrate with a cylindrical circular hole. Widely used Cu catalyzed CVD-growth of graphene [1] and wet transfer technique using PMMA coating [2] were employed for the sample preparation.
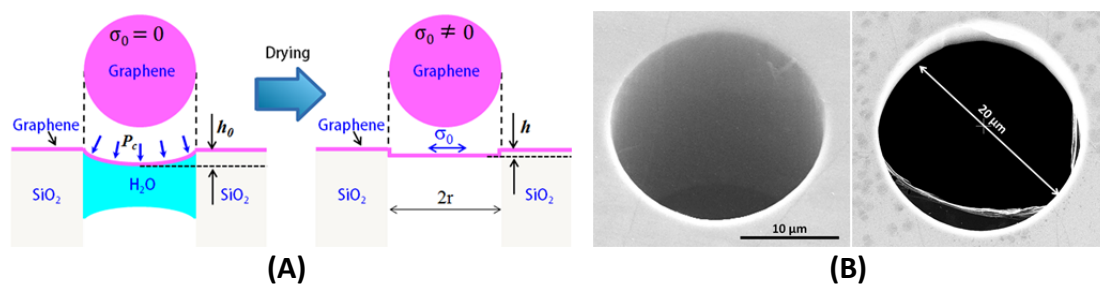

Figure S2. Graphene membrane suspended on Si substrate with a cylindrical hole. (A) Generation of residual biaxial tension by the stiction phenomenon. For the preparation of fully suspended graphene membrane, water had been used for rinsing. It had been observed that rinsing with water and subsequent drying procedures induce the stiction between the graphene and the vertical wall of the hole, presumably due to the attractive capillary force and van der Waals force. (B) Left image shows a scanning electron micrograph of successfully suspended graphene membrane on Si substrate. Due to the unavoidable mechanical stress developing during wet etching and drying process, the graphene membranes have often broken (right image).
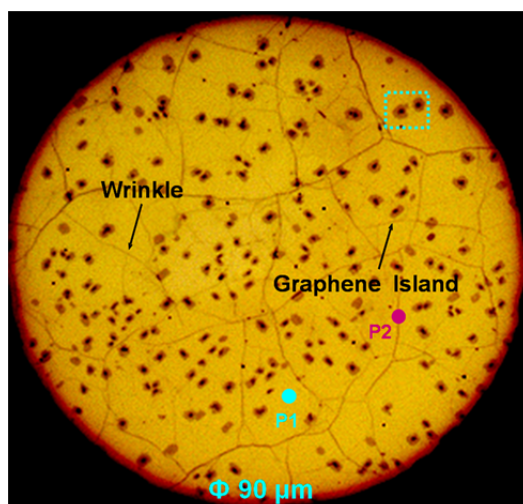
Figure S3. **False colored optical microscope image of the suspended monolayer CVD-graphene**. In order to make wrinkles and islands to be easily identified, the color contrast was adjusted.
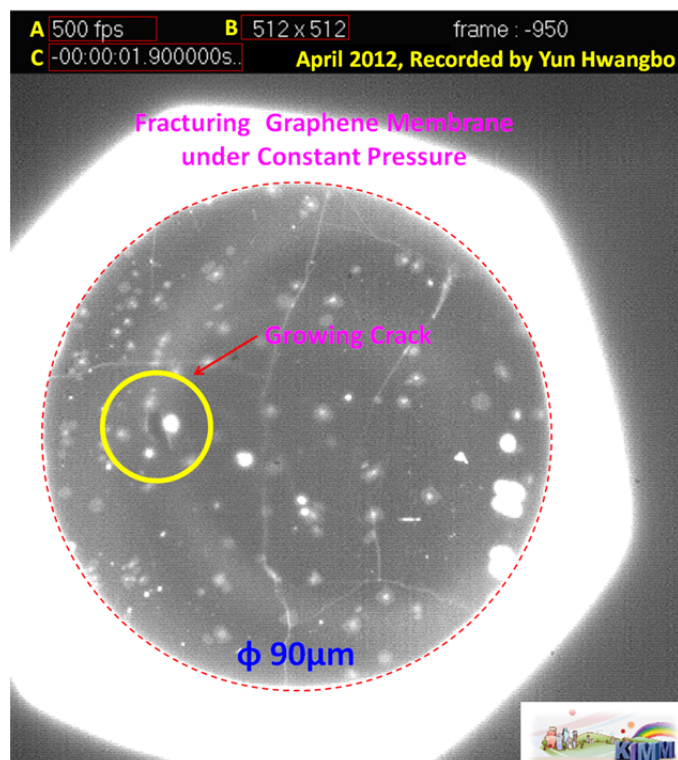

Figure S4. A snapshot of the motion picture in the Supplementary Information (Movie S1). The movie was produced with 500 frames per second (A) and the frame size of 512 x 512 pixels (B). The time-display showing the elapsed time has a format of hh:mm:ss. The current elapsed time is 1.900000 seconds (C).
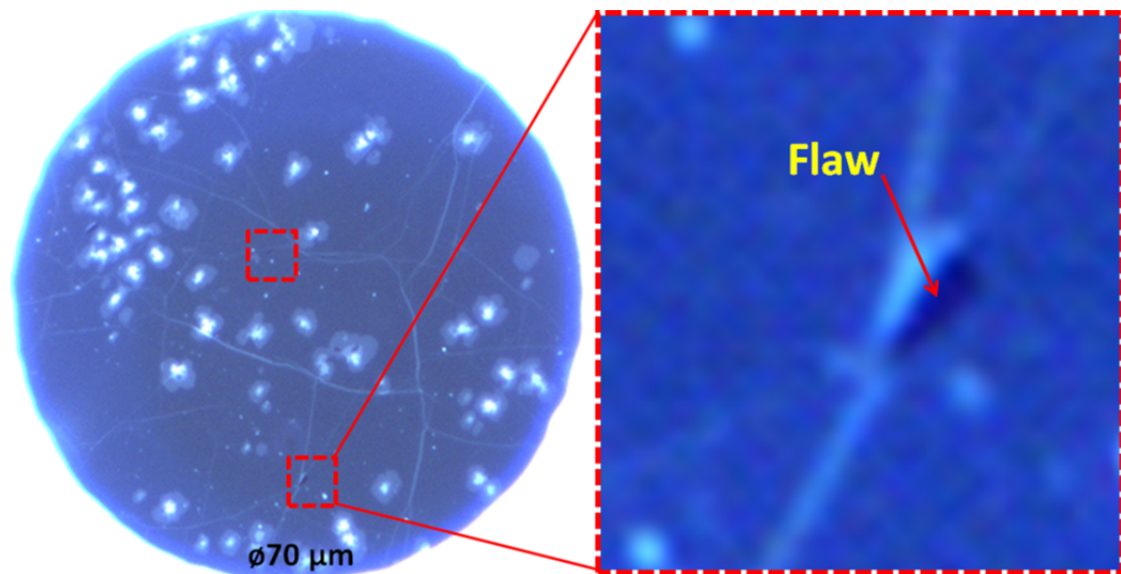
Figure S5. **Optical microscope images of pinholes observed on the suspended graphene.** The pinholes are currently considered to be presumably by inter-domain merging taken placed on the CVD growth or by transferring graphene onto Si substrate. These pinholes are believed to be another feasible crack initiation source together with topological defects of the CVD-graphene. So far, on the prepared suspended graphene membranes, diversely shaped pinholes (e.g., circular, elliptical, triangular, and sharp lined pinholes) have been observed and the size distribution has been also quite broad (from few nanometers to few micrometers).
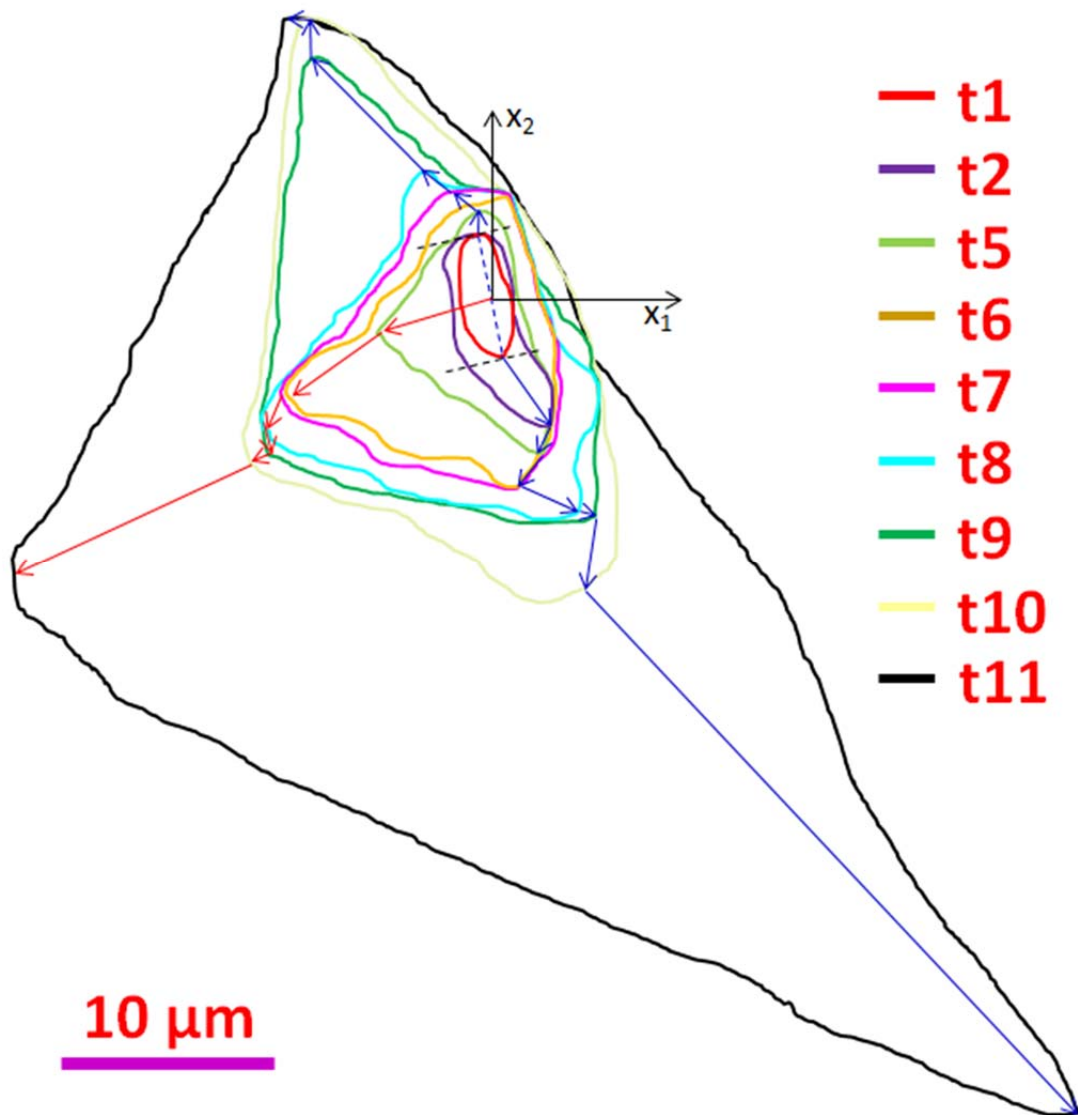
Figure S6. Exemplified image for the identification of the crack propagation path and the measurement of the crack extension length. For the precise measurement of length of cracks (a1 and a2), a built-in software in the optical microscope (Eclipse Ni-E, Nikon) was used. Firstly, the cracked areas in the instant images of the fracturing graphene taken with high speed camera were carefully articulated using the optical microscope software tool. The projected lineal distances between cracked edges were carefully measured to be crack length in both mother crack (crack 1, a1) and branched crack (crack 2, a2), shown in Figure 2B as an example. The crack length extension histories were graphically processed (Figure 2C).

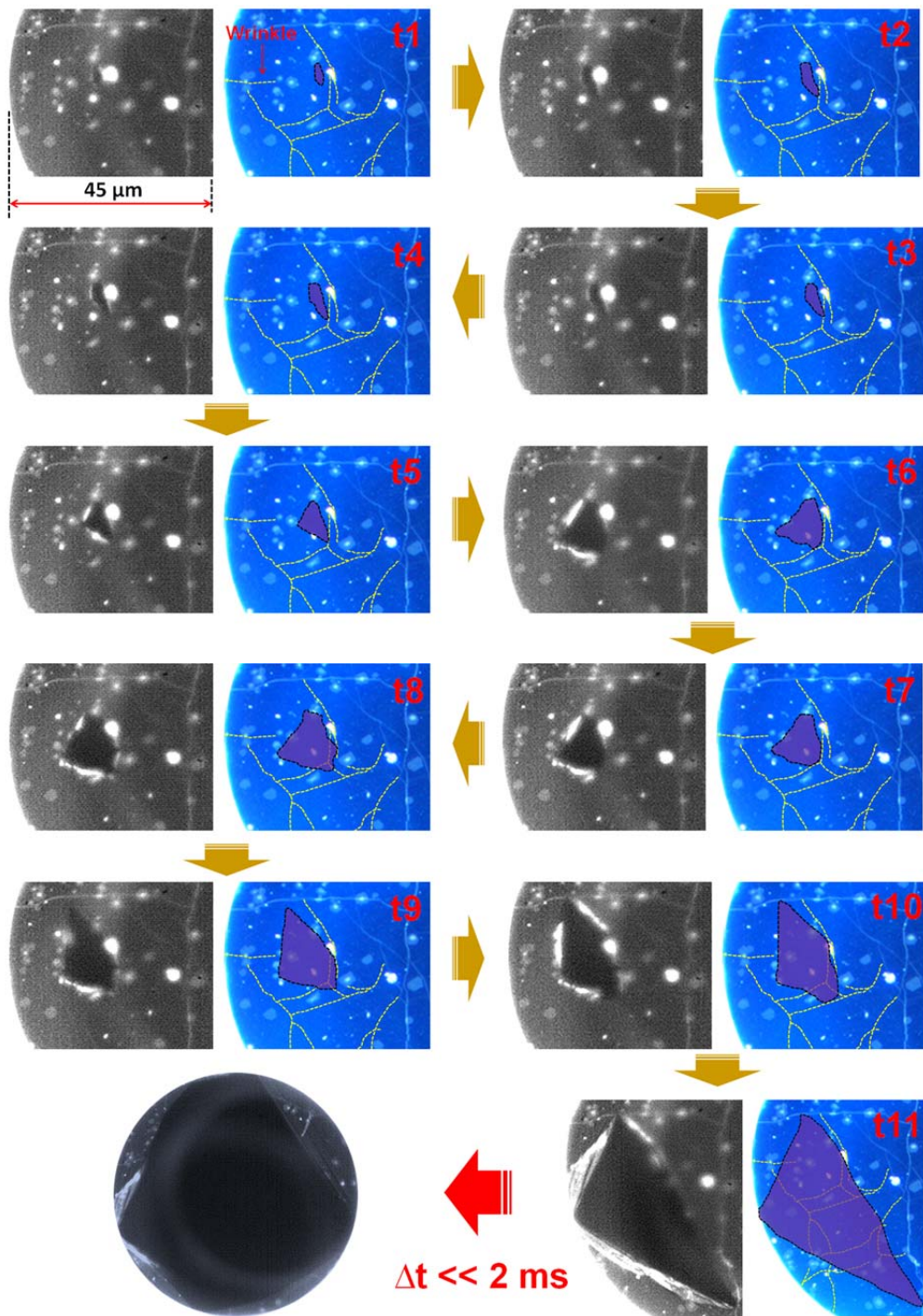**Figure S7. Crack propagation history and image processing for measurement of the crack length.** As mentioned in Figure S6, the cracked areas in the instant images of the fracturing graphene taken with a high speed camera were carefully articulated using the optical microscope software tool. In each pair image, the left is an image taken from high speed camera and the right is a corresponding optical microscope image, respectively.
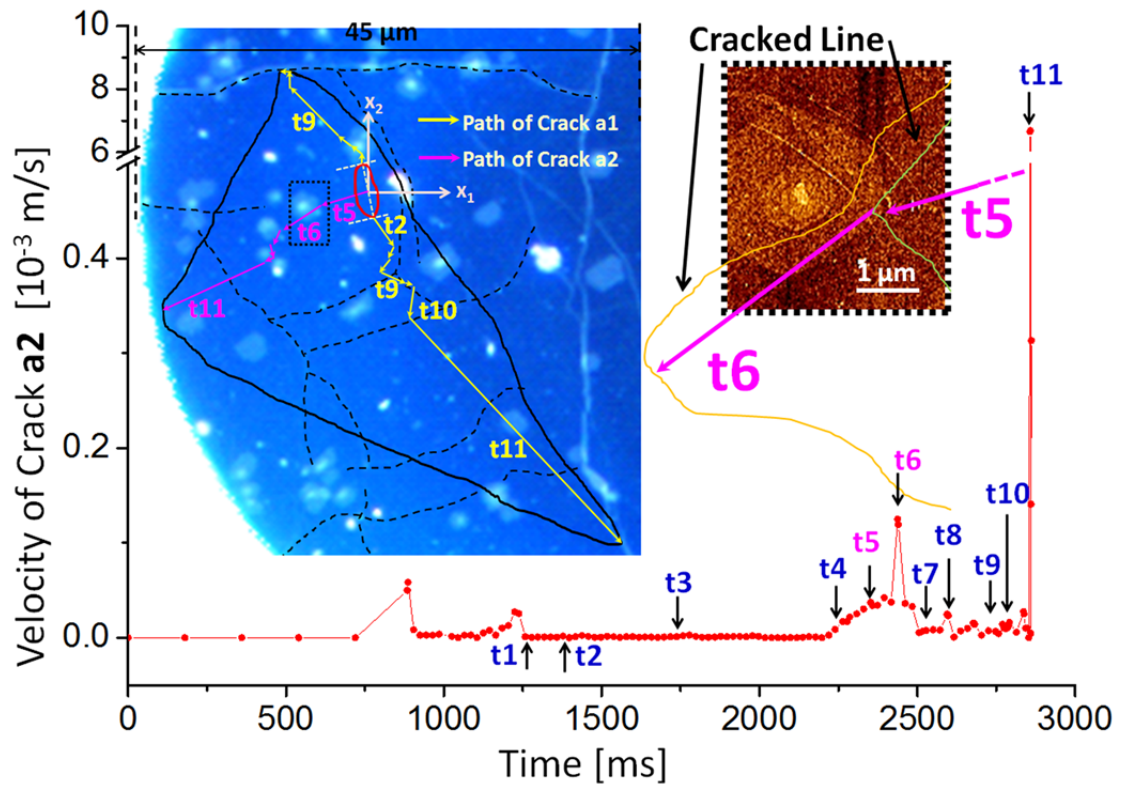
Figure S8. Crack propagation velocity diagram of the branched crack (a2) and crack arresting. Similar to the mother crack (a1), the propagating branched crack was observed to be arrested mostly due to the thickness differences, as can be recognized from the red-colored dotted circle in Figure 2D. More interestingly, the propagating cracks were observed to detour the thick regions on the CVD-graphene instead of penetrating through. As depicted in the inset AFM image of the thick graphene island with overlapped crack lines, the crack running from t5 to t6 was found to distinctly bypass.

Figure S9. Schematic stress intensity factor (K_I) versus crack velocity (V) diagram ($V - K_I$ plot) for subcritical crack growth due to stress corrosion [3]. K_{Ic} is the fracture toughness and K_{th} is the threshold of stress corrosion crack growth. Based on the Charles's power law [4,5], the curve can be described as an empirical formula, $V = V_0 \exp(-H/RT)K_I^n$, where V is the crack vel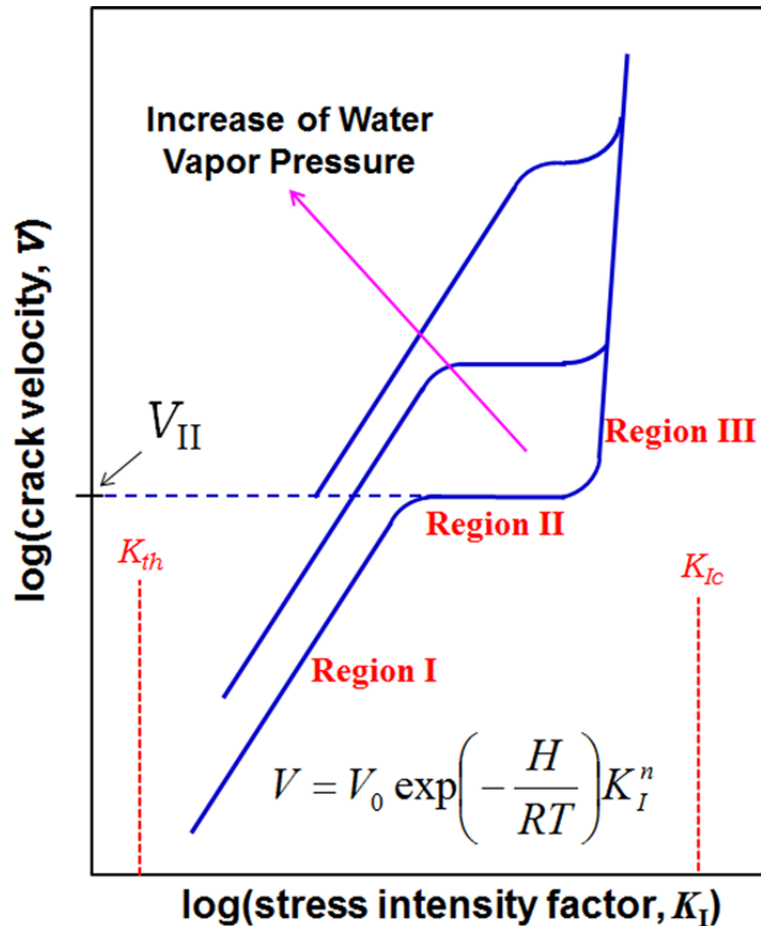ocity, H is the activation enthalpy, R is the gas constant, T is the absolute temperature, V_0 and n are constants, respectively. Simply, the curve can be described as $V = AK_I^n$ where, A and n are crack growth parameters, respectively. In region **I**, subcritical crack growth is controlled primarily by the rate of stress corrosion reactions at crack tips and crack velocity increases exponentially with applied load as well as humidity; whereas in region **II**, the growth is controlled by the rate of transport of reactive species to the crack tips and thus crack velocity is independent of applied stress but depends on humidity. In region **III**, the growth is controlled by thermally activated bond rupture which is largely independent of chemical environment, accordingly, the crack velocity is independent of humidity but depends on applied load [6].
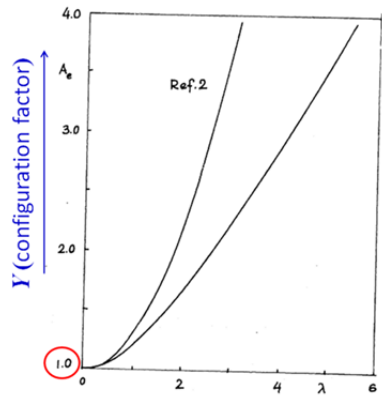
Figure 3. Stress intensity ratio in sphere ($N_0 \neq 0, M_0 = 0$)

Figure S10. Configuration factor(Y) for spherical shell reported in literature. This figure is extracted from reference 74 and modified. y axis indicates configuration factor (Y), λ in x axis defines the shell parameter, i.e. $\lambda = [12(1 - v^2)]^{1/4} a \sqrt{Rt}$, where v, a, R and t are Poisson's ratio, crack length, curvature of shell and shell thickness, respectively.
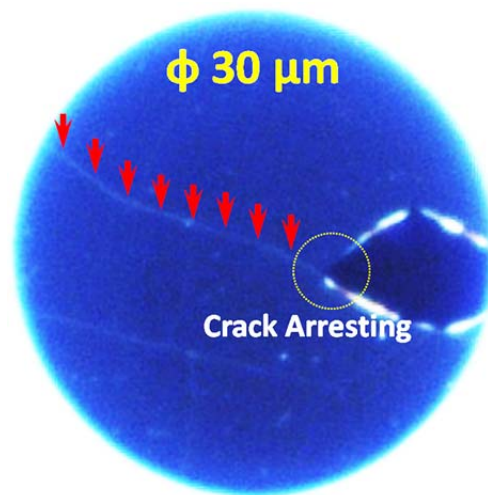
Figure S11. Optical microscope image of the naturally fractured CVD-graphene in room condition. Although initially the prepared CVD-graphene membrane remained fully covered and well suspended on Si substrate, as shown in figure, it has been too often observed to start fracturing in a few days or even in a few hours after leaving as it is in room condition. Most of the fractured graphene membranes have showed the state that the propagating crack is arrested by the graphene wrinkles or islands. The red arrows indicate the graphene wrinkle.
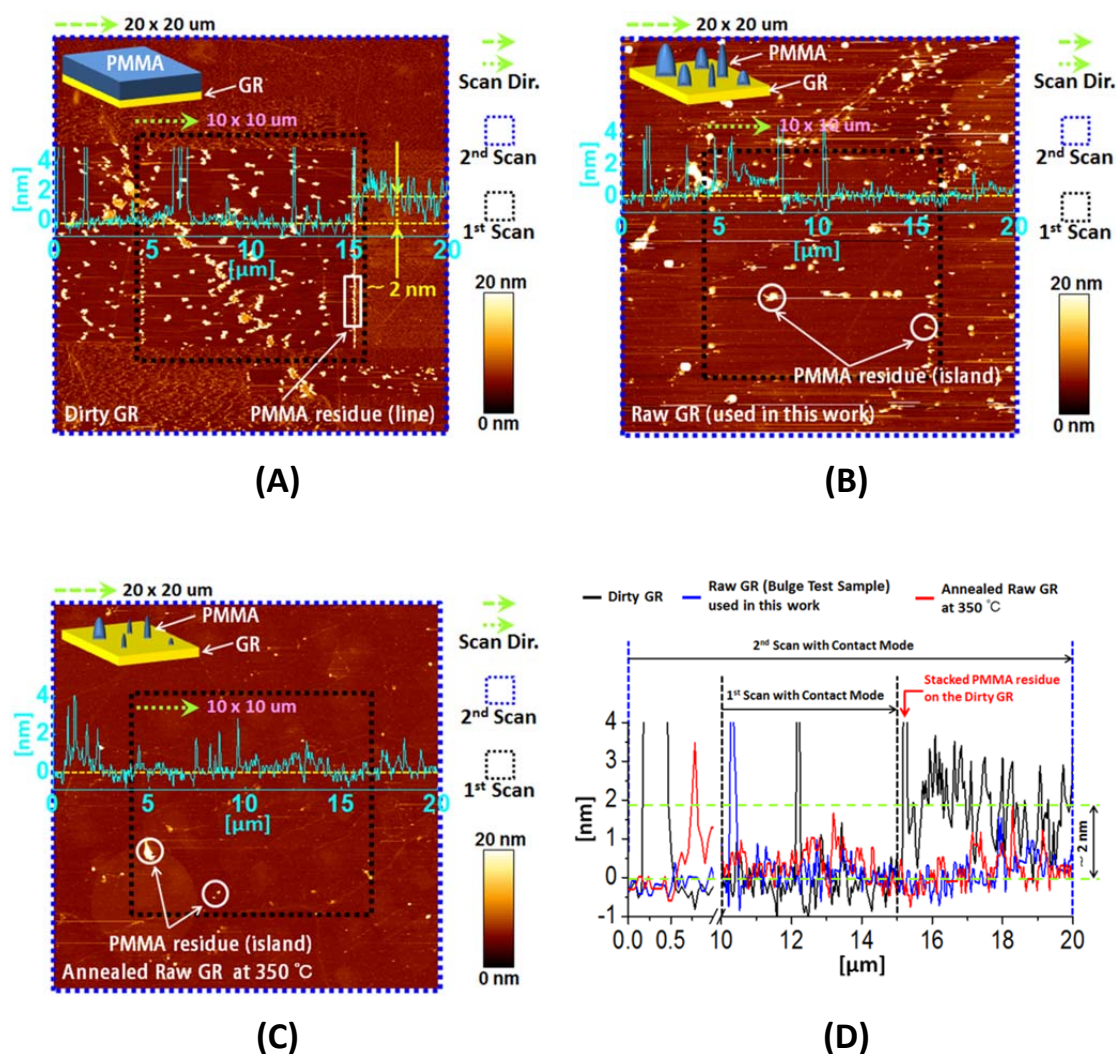
Figure S12. AFM investigation results showing amount and distribution of the PMMA residues on the CVD-graphene samples. Referring to the reports in literature [77,78], in order to estimate the amount of the PMMA residues remaining on our transferred CVD-graphene samples onto SiO$_2$ substrate (GR/SiO2), firstly, arbitrary regions (10 μm x 10 μm) on the graphene samples (GR/SiO2) were selected. Then, AFM (NanoWizard® II, JPK Instrument) scanning was performed over the sample surface using a contact mode AFM tip, which was adjusted to be contacted with the sample surface. The contact force of the tip was 5 nN, which was controlled to be lowest possible and constant while scanning. Subsequently, additional scans over the larger regions (20 μm x 20 μm) including the previously scanned regions were carried out with non-contact mode. The scanning frequency had been 0.3 Hz. The dotted boxes with black color (10 μm x 10 μm) / with blue color (20 μm x 20 μm) of each image indicate 1st / 2nd scanned regions of each sample, respectively. By scanning, the AFM tip scraped the PMMA residues including other contaminants off the graphene sample surface. **(A)** "Dirty Graphene" commonly cited in literature, it is fully covered with the continuous PMMA residue film with the thickness of ~2

nm. The scraped PMMA residues were neatly accumulated on the right and left of the black dotted box, thereby building up the PMMA residue wall. **(B)** Unannealed graphene sample which was used in bulge test for this research. As compared to the "Dirty Graphene", the sample quality shows better quality. One distinctive feature of this sample is that the PMMA residues markedly exist in the form of island shape, not continuous film. **(C)** Annealed graphene sample (the sample **(B)** was annealed at 350 °C in a vacuum). As can be figured out, the amount of the PMMA residues appeared to be conspicuously decreased by annealing. However, despite of such annealing, the PMMA residues were observed to still remain on the graphene surface. **(D)** Comparison of height profile (cyan colored line in each figure). In the case of the "Dirty Graphene", it had been observed that the graphene is covered with the PMMA residue with the thickness of around 2 nm. In the other two samples, on the other hand, the height profiles do not show clear differences. It indicates that although our unannealed samples used in bulge test experiment have higher distribution density and amount of the PMMA residues than the annealed graphene samples, the unannealed samples are also sparsely dotted with the PMMA residue islands similar to the annealed samples. To be short, AFM investigation showed that the "Dirty Graphene" is fully covered with the PMMA residue layers with the thickness of ~2 nm and the bonding force between the residue and the graphene is fairly weak.
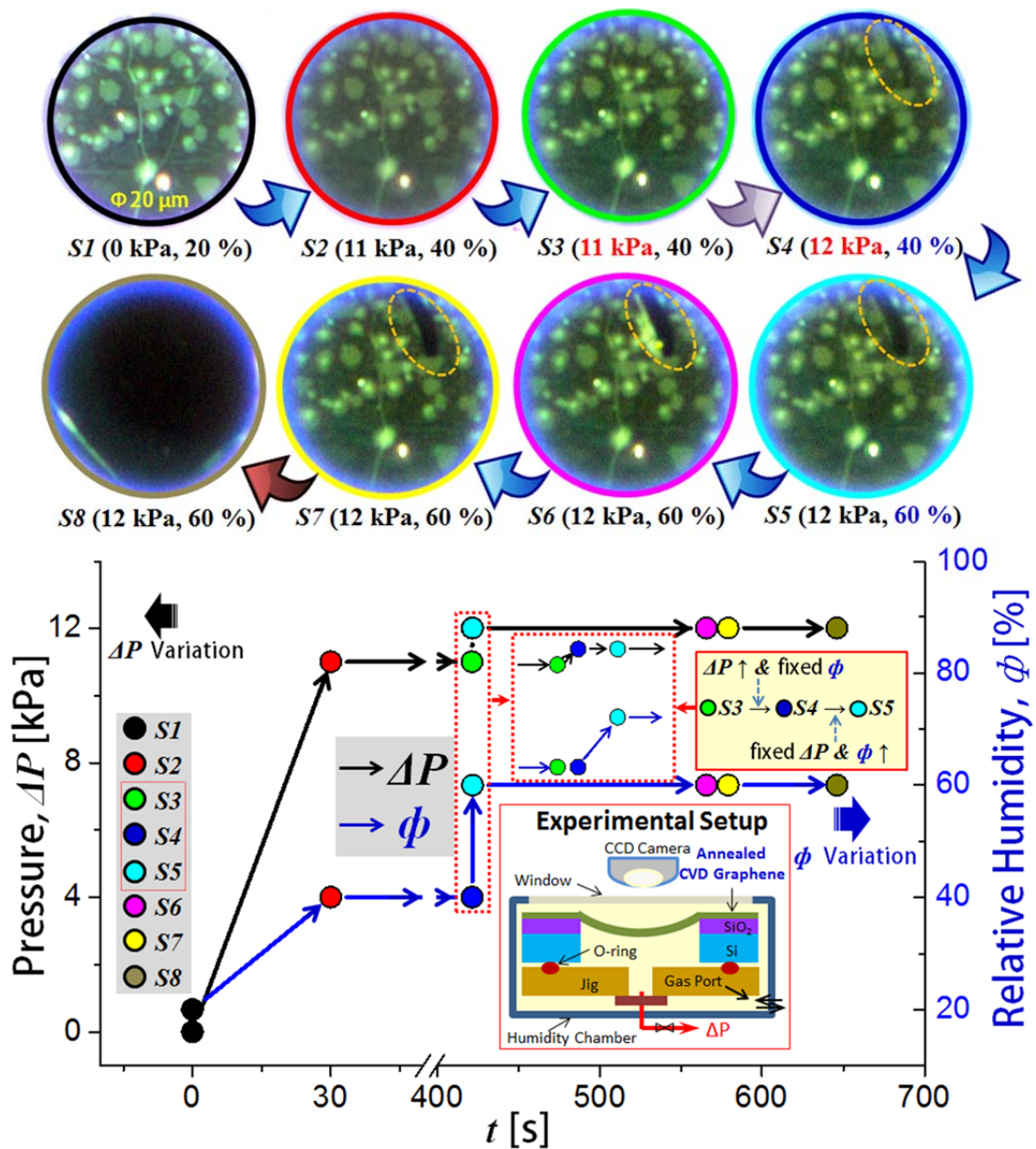
Figure S13. Fracture behavior of the annealed CVD-graphene under the condition of fixed/increased humidity and increased/fixed pressure, respectively. Unlike experiment shown Figure 4B, in this experiment, pressure and humidity was alternatively adjusted from $S3$ to $S5$. Firstly, fracture behavior was observed under the condition of increased pressure and fixed humidity, i.e. $S3$(11 kPa, 40 %) → $S4$(12 kPa, 40 %). As can be seen from optical microscope images, minimum detectable crack appeared due to the pressure increase. Further increase in humidity [$S4$(12 kPa, 40 %) → $S5$(12 kPa, 60 %) led to acceleration of subcritical crack growth of the graphene (see the Movie S3).
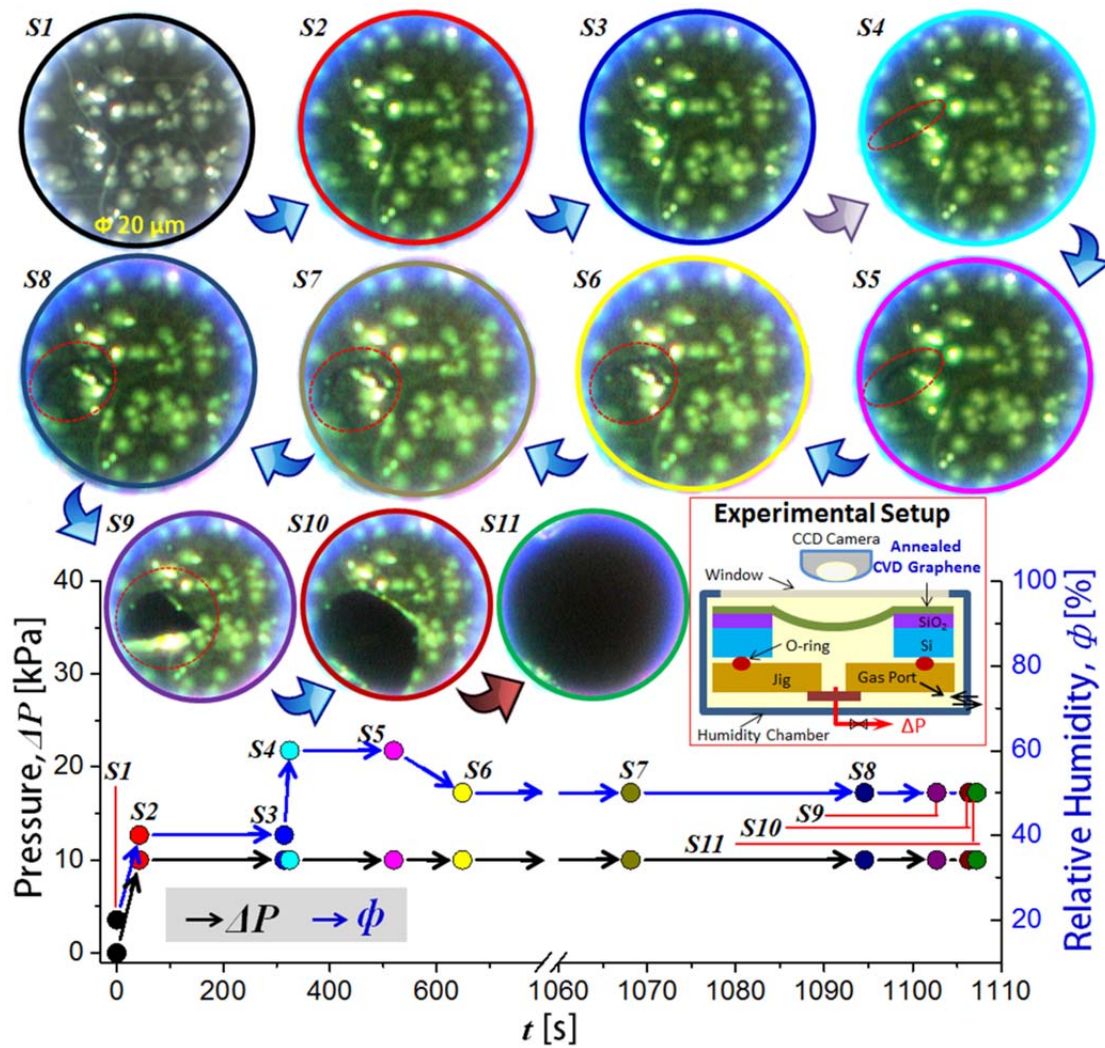
Figure S14. Fracture behavior of the annealed CVD-graphene under the condition of varying humidity. Firstly, it was able to confirm that minimum detectable crack appears due to the humidity increase [*S3*(10 kPa, 40 %) → *S4*(10 kPa, 60 %)]. Subsequently, the humidity was adjusted to be reduced [*S5*(10 kPa, 60 %) → *S6*(10 kPa, 50 %)]. As can be recognized from optical microscope images and corresponding time scale, initiated crack appeared to more quickly propagate under 60 % humidity (*S4* → *S5*) than 50 % humidity (*S6* → *S8*) (see the Movie S4).
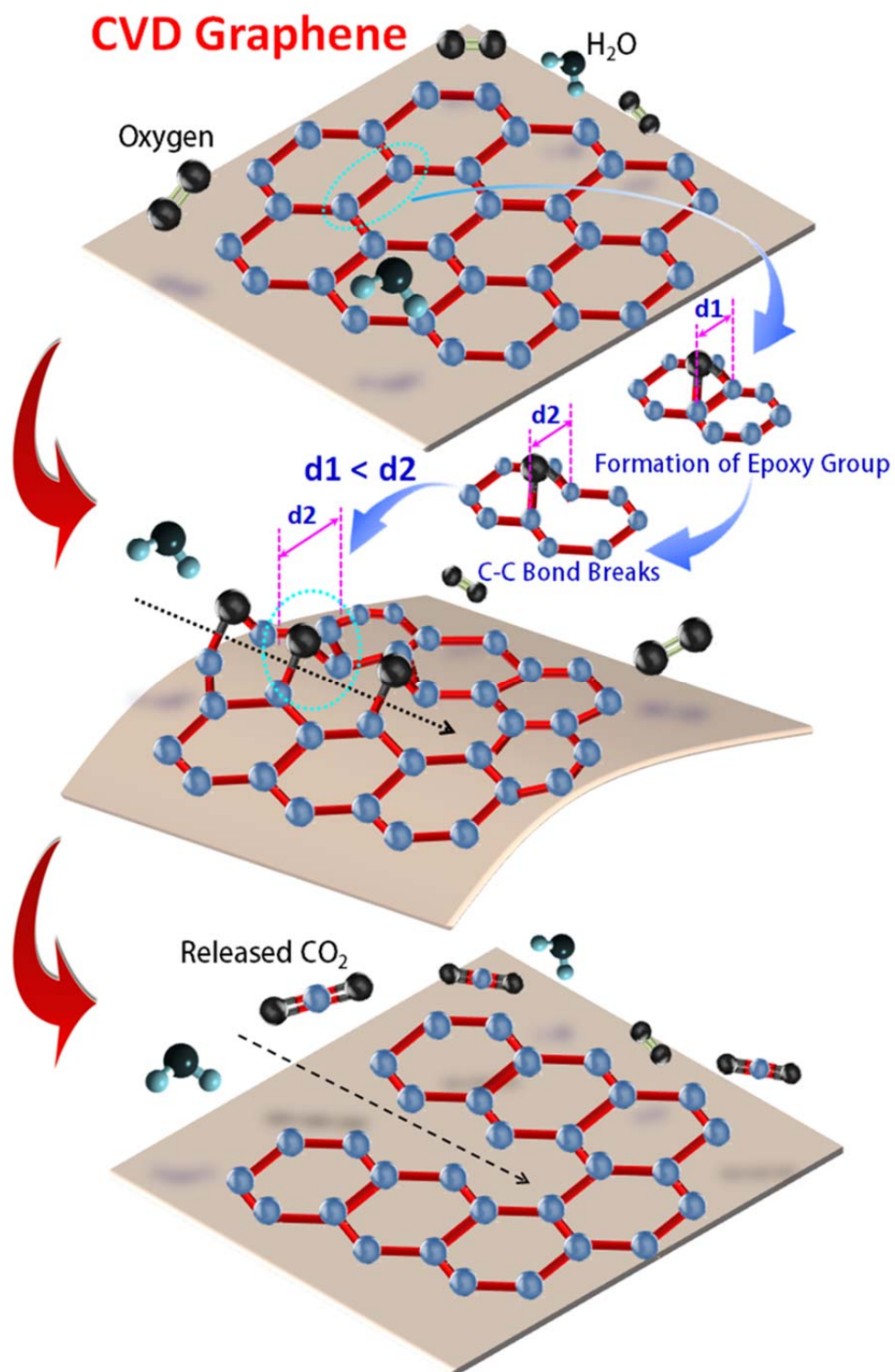
Figure S15. Atomistic model describing the crack initiation/propagation or defect formation by configuration change. See the details in the text.
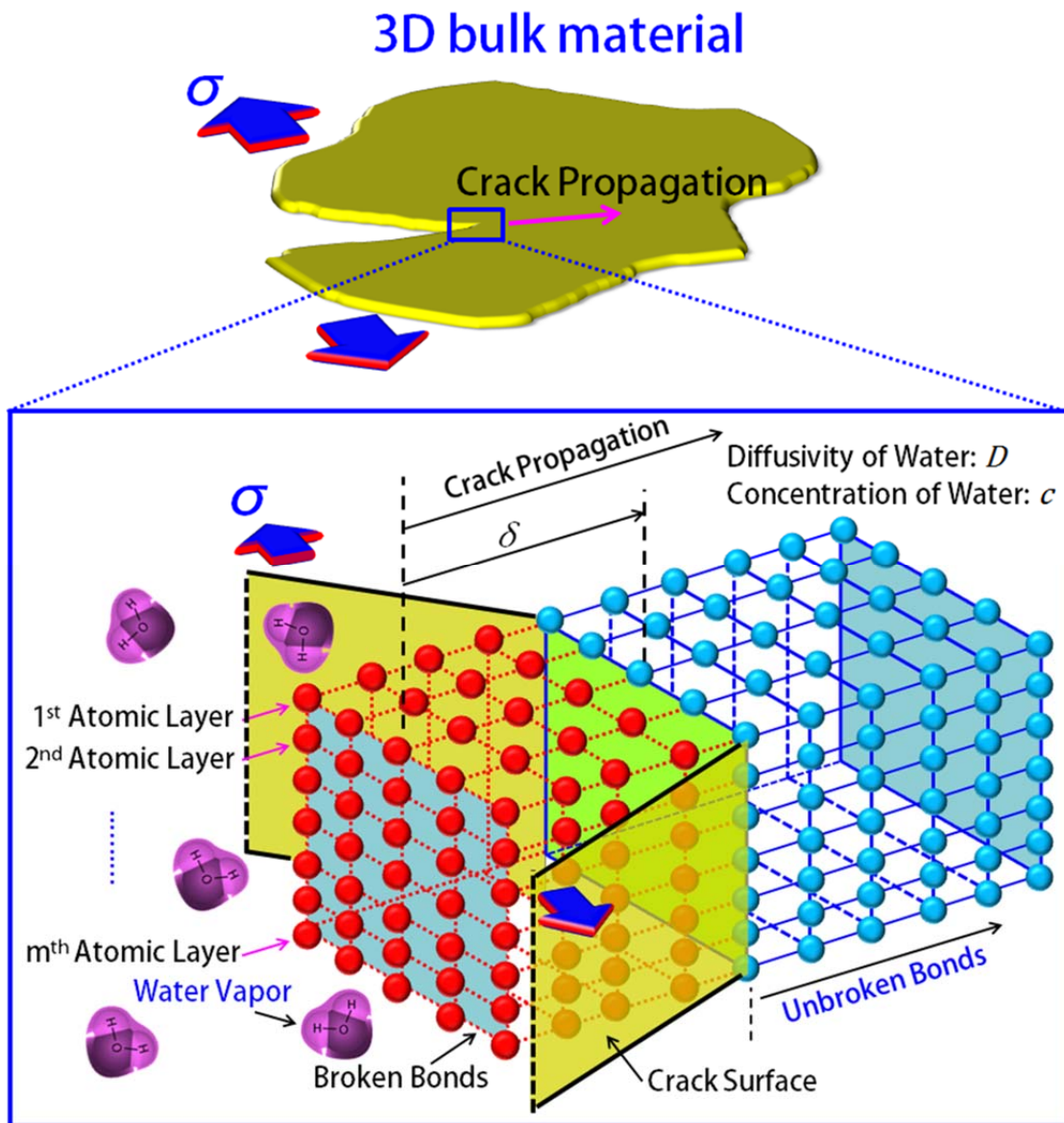
Figure S16. Schematic 3D atomic structure model describing the diffusive transport of water vapor to the crack tip surface. In case of one dimensional diffusive transport model of the water vapor in the monolayer structure, Wiederhorn reported that the crack velocity (V) could be described as, $V \sim \frac{cD}{\delta n}$, where c and D are the total concentration and the diffusivity of H_2O vapor, δ is diffusive boundary layer thickness, n is the order of chemical reaction (n molecules of water are required to break a single bond in the monolayer, i.e. $n H_2O$ + Bond $\rightarrow$ Broken Bond) [7]. The crack velocity of the 3D bulk material with m atomic layer structures ($m > 1$) can be easily deduced as $V \sim \frac{cD}{\delta n m}$.
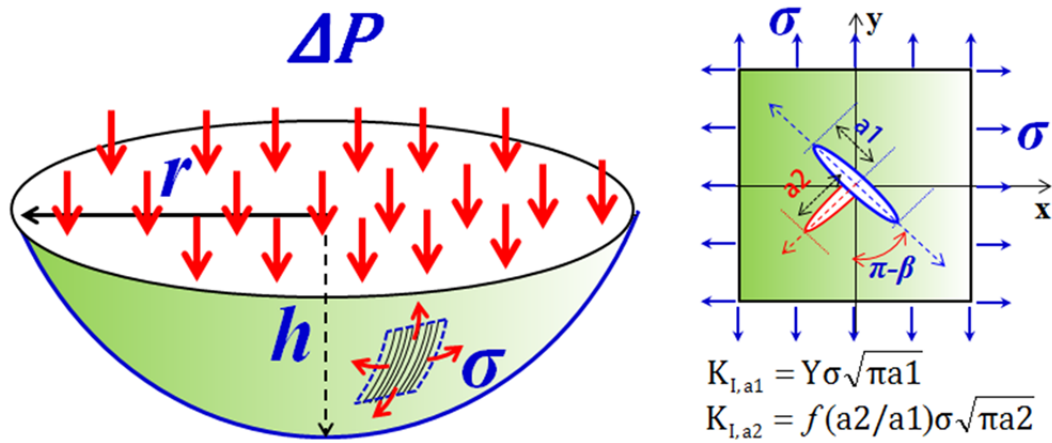
Figure S17. Schematic description of inverse bulge test and relevant parameters. In the left figure, ΔP, r, h and σ denote applied pressure, radius of membrane, deflection and nominal radial stress, respectively. The right figure shows stress intensity factors of a mother crack (center crack, the crack length = 2a1) and a branched crack (edge crack, the crack length = a2) under biaxial stress state. The detailed discussion can be found in Supplementary Discussion **IV**.

2. Supplementary Tables

Table S1. Dataset successfully obtained from the bulge test of the suspended monolayer CVD-graphene membrane on Si substrate with a various sized cylindrical circular hole. $K_{I,A}$ denotes a maximum stress intensity factor calculated based on the observed maximum crack length (see "A" marked in Figure 2C, for reference) before catastrophic failure (see "B" marked in Figure 2C). Each K_{Ic} value was estimated from asymptote of convergence in each interpolated trimodal curve of the corresponding dataset (see Figure 3 as an example). Since the minimum resolution of the high speed camera used in this study was 2 ms, some interim images showing fracture behaviors likely existing between state A and state B (see Figure 2C) may have been omitted. Therefore, the estimated K_{Ic} values could have slight variances.

	Sample	Hole Diameter [μm]	Crack Length, 2a [μm]	ΔP [kPa]	σ [GPa]	$K_{I,A}$ [MPa m$^{1/2}$]	Expected K_{Ic} [MPa m$^{1/2}$]
Without Annealing	G1	10	7	36.0	2.22	7.3	8.5
	G2	30	18	4.0	1.06	5.6	6.5
	G3	30	20	5.0	1.23	6.8	7.9
	G4	70	20	3.0	1.54	8.6	10.0
	G5	90	49	2.0	1.39	12.1	14.1
	G6	90	54	2.0	1.39	12.7	14.8
	G7	90	63	1.5	1.15	11.4	13.3
With Annealing at 250 ℃ †	G8	20		11.0			
	G9	20		12.0			
	G10	20		10.0			
Average ± Standard Deviation						9.2 ± 2.8	10.7 ± 3.3

† As mentioned in experimental section, the fracturing behavior of the unannealed graphene membrane was recorded using high speed camera (Fastcam 1024 PCI, Photron) at the speed of 500 fps. However, in the case of the annealed graphene membranes, due to the long duration of crack propagation and limitation of recording capacity, high speed camera was not able to be used. Unavoidably, the fracturing behaviors were recorded using CCD camera (DS-Fi2, Nikon) at the speed of 37 fps. For this reason, proper images capturing a moment just before catastrophic failure were not able to be taken. Nevertheless, those captured images proximate to the catastrophic failure were able to be used to calculate stress intensity factors. However, those images could result in largely erroneous stress intensity factor because of the underestimated crack length. Hence, the stress intensity factor and relevant fracture toughness from the annealed graphene membranes were excluded in the table.

Table S2. Raman shift data of the suspended monolayer CVD-graphene membrane on Si substrate with cylindrical circular hole.

Position	I_D/I_G	I_{2D}/I_G	ω_G (cm^{-1})	ω_{2D} (cm^{-1})
Substrate	0.048	1.646	1586.5	2689.0
P1	0.049	3.802	1577.6	2666.9
P2	0.048	3.226	1578.2	2666.1
P3	0.032	1.018	1577.6	2690.3
P4	0.031	0.785	1574.6	2689.0

Table S3. Fracture toughness (K_{Ic}) of the some engineering materials.

Materials	(Mode I) Fracture Toughness, K_{Ic} [MPa m$^{1/2}$]
Metallic Materials	
Mild steel [8]	140
High strength steel [8]	50-154
Cast iron [8]	6-20
Pure ductile metals (Al, Cu, Ag, etc) [8]	100-350
Beryllium [8]	4
Ductile iron [8]	45.3
High carbon steel [9]	30
Low carbon steel [10]	41-82
Stainless steel [10]	62-280
Alloys [10]	
Copper alloy	30-90
Lead alloy	5-15
Magnesium	12-18
Nickel alloy	80-110
Zinc alloy	10-100
Aluminum alloy	22-35
Titanium alloy	14-120
Low alloy steel	14-200
Ceramics	
Alumina [8]	2.7-4.2
Silicon carbide (sintered) [8]	4.8
Silicon carbide (hot pressed) [8]	5.2
Silicon nitride(hot pressed) [8]	4.1-6.0
Silicon nitride (reaction bonded) [8]	3.6
Silicon nitride (sintered) [8]	5.3
Boron carbide [10]	2.5-3.5
Silicon [10]	0.83-0.94
Tungsten carbide [10]	2.0-3.8
Aluminum nitride [10]	2.5-3.4

Polymers	
Nylon 6,6 [8]	2.5-3
Polycarbonate (PC) [8]	2.2
Polymethylmethacrylate (PMMA) [8]	0.7-1.6
Polystyrene (PS) [8]	0.7-1.1
ABS Polystyrene (PS) [9]	4
Polyvinyl chloride (PVC) [8]	2.0-4.0
Polyethylene (PE) [8]	1-6
Polyethylene terephthalate (PET) [8]	5
Butyl rubber [10]	0.07-0.1
Ethylene-vinyl acetate (EVA) [10]	0.5-0.7
Isoprene (IR) [10]	0.07-0.1
Natural rubber [10]	0.15-0.25
Neoprene [10]	0.1-0.3
Polyurethane elastomer [10]	0.2-0.4
Silicon elastomers [10]	0.03-0.5
Acrylonitrile butadiene styrene (ABS) [10]	1.19-4.30
Cellulose polymer [10]	1-2.5
Ionomer [10]	1.14-3.43
Polyetherketone (PEEK) [10]	2.73-4.30
Telfon (PTFE) [10]	1.32-1.8
Epoxy [10]	0.4-2.22
Phenolics [10]	0.79-1.21
Polyester [10]	1.09-1.70
Others	
Co/WC metal matrix composites [9]	14-16
Concrete (steel reinforced) [9]	10-15
Concrete (unreinforced) [9]	0.2
Glass [10]	
Borosilicate glass	0.5-0.7
Glass ceramic	1.4-1.7
Silica glass	0.6-0.8
Soda-lime glass	0.55-0.77
Aluminum/silicon carbide [10]	15-24
Glass fiber reinforced polymer (GFRP) [10]	7-23
Carbon fiber reinforced polymer (CFRP) [10]	6.1-88
Brick [10]	1-2
Rock [9]	1
Woods (perpendicular to grain) [9]	11-13
Woods (parallel to grain) [9]	0.5-1.0
Bamboo [10]	5-7
Leather [10]	3-5
Cork [10]	0.05-0.1

Carbon Based Materials	
Diamond (natural) [11]	3.4
Diamond (CVD diamond) [12]	5-6
Graphite (Bulk) [13]	1.4
Carbon nanotube	?
Graphite sheet (Theory) [14]	4.7
Graphene (Theory)-Armchair [15]	3.37
Graphene (Theory)- Zigzag [15]	4.21
CVD-Graphene (Our result from experiment)	10.7 ± 3.3

Table S4. **Experimentally measured subcritical crack growth rate at region II in Figure S9 (V_{II}) of diverse materials under fracture mode-I.** RT: Room Temperature, RH: Relative Humidity, P_{H2O}: Water Vapor Pressure.

Materials	V_{II} [m/s]	Condition	Ref.
Partially stabilized ZrO_2(MgO)	$\sim 10^{-4} - 10^{-3}$	T = 22 °C, RH = 55 %	[16]
Soda-lime glass	$\sim 10^{-4}$	RH = 30 %, RT	[7]
Fused silica glass	$\sim 10^{-5}$	T = 25 °C, P_{H2O} = 120 kPa	[17]
Phosphate glass	$\sim 10^{-7} - 10^{-6}$	T = 15 °C, P_{H2O} = 270 kPa	[17]
Al_2O_3	$\sim 10^{-4}$	Room conditions	[18]
ZrO_2	$\sim 10^{-4}$	Room conditions	[19]
Al_2O_3-10% ZrO_2	$\sim 10^{-5} - 10^{-4}$	Room conditions	[20]

3. Supplementary Discussion I

It has been well accepted that the red(down)/blue(up) shifts of Raman vibrational bands, G and 2D, are also sensitive to substrate [21], doping [22-33], and temperature [34-37], besides strain effect [38-45]. As can be seen in Figure 1C, both G and 2D mode measured from the suspended graphene are observed to be redshifted (downshifted) as compared to those modes measured from the graphene on the SiO$_2$ substrate. Conversely, G and 2D mode measured from the graphene on the substrate are observed to be blueshifted (upshifted) as compared to modes measured from the suspended graphene.

Firstly, concerning Raman spectra of the graphene placed on SiO$_2$ substrate, it has been recently reported that Raman feature is irrelevant to the surface properties of substrate [21]. In particular, the SiO$_2$ substrate plays a negligible role in affecting the atomic/electronic structure of the graphene. Considering that the substrate effect is insignificant, the Raman peak shifts observed in our sample could be believed to be most likely caused by doping from the underlying SiO$_2$ substrate. It has been reported that in the substrate-dependent doping, surface dangling bonds meditate the chemical coupling reaction to the graphene and the dangling bonds can lead to p(hole) or n(electron) doping via charge transfer [47] even in the absence of extrinsic impurities in substrate [48]. In particular, graphene is p doped by oxygen dangling bonds on the SiO$_2$ substrate, whereas n doping takes place by silicon dangling bonds [48, 49]. p and n dopings induce not only shifts of Dirac points in ambipolar curves for graphene based devices but also distinct shifts in G and 2D Raman bands. In other words, it has been reported that p doping causes blueshift (upshift) for both G and 2D bands, while n doping results in opposite shifting in G and 2D bands [e.g. blueshift (redshift) in G /redshift(blueshift) in 2D] [28-31]. Thus, the graphene placed on SiO$_2$ substrate can exhibit not only blueshifted G and 2D peaks, but also oppositely shifted G and 2D peaks.

Secondly, concerning Raman spectra of the suspended graphene, as can be seen in Figure 1C, no splitting of the G peak and splitting/broadening of the 2D peak are observed. In addition, the position of G peak is shifted from 1586 to 1577 cm^{-1} (redshift, Δw_G = -9 cm^{-1}), and 2D peak moves from 2689 to 2666 cm^{-1} (redshift, Δw_{2D}

= -23 cm^{-1}) when moving from the substrate to the cylindrical hole. The full width half maximum value of 2D peak remains nearly unchanged. Regarding to these redshifted G and 2D peaks, as mentioned above, three different explanations are possible, i.e. doping, temperature, and strain. Among these factors, the temperature effect can be ruled out since any annealing effect was not involved in the preparation of the sample. Doping, as mentioned, leads to blueshifts of both G and 2D peaks (p doping) or opposite shifts of G and 2D (n doping). Considering the recent report that the ratio ($\Delta w_{2D}/\Delta w_G$) related to p doping effect is around 0.7 (in our case, $\Delta w_{2D}/\Delta w_G$ > 2.5)[50], the doping effect is also thought to be minor. Hence, the observed redshifts in our Raman spectrum is believed to be closely related to biaxial tensile strain [2, 38-40, 45-46], which is typically observed when the graphene is decoupled from the underlying substrate.

4. Supplementary Discussion II

The crack travelling path in the graphene is thought to be closely related to intergranular (along the grain boundary) / transgranular (across the grain boundary) fracture path frequently observed in bulk materials. The travelling path is determined by the inherent microstructure of material. It is well known that the crack path can be decided by the interaction between microstructure and environmental conditions, such as stress corrosion cracking. Firstly, in the transgranular crack propagation, the crack travels through the grain (across the grain boundary) of the material. The travelling crack changes direction from grain to grain due to the different lattice orientation of atoms in each grain. In other words, when the travelling crack reaches a new grain, it has to find a new path or plane of atoms to travel on because it is easier to change the path to the direction with least resistance than it is to rip through. In contrast, in intergranular fracture, the crack travels along the grain boundaries, and not through the grains. Intergranular fracture usually occurs when the phase in the grain boundary is weak and brittle. Considering the fact that the CVD-graphene is a polycrystalline and microstructured material, the tendency of crack propagation in CVD-graphene may be able to be figured out to some extent, although it is difficult to predict the exact crack path. It has been

recently reported that, in room condition the cracks in graphene propagate along the grain boundary [51], while in vacuum condition the graphene tears crossing grain boundary [52]. In other words, intergranular or transgranular fracture in CVD-graphene are considered to be largely determined by the environmental conditions.

5. Supplementary Discussion III

Generally, in the case of dynamic fracture behavior of materials, crack growth could be accompanied by dynamic crack branching and curving caused by dynamic instability of the crack tip [53,54]. In particular, in the case of brittle materials, a propagating crack shows strong branching/curving tendency. Depending on stress state, the crack departs from its original trajectory and curves or splits into two or more branches. The study on crack curving and branching criteria has been intensively performed in dynamic fracture mechanics. The precise criteria have been still a subject under debate. In the past, some researchers attempted to explain the crack branching in terms of kinetic energy. If the kinetic energy were consumed for the crack branching, the velocity of cracks would decrease. However, real time investigation on dynamic crack branching has shown that the branching does not alter the crack velocity [55]. As an alternative, critical stress intensity criterion has been widely-accepted so far [56-60]. The criterion says that the crack branching under mode $\mathbf{I}$ loading occurs only when a specific stress intensity factor is exceeded. In other words, it can be stated as

$$K_I \geq K_{Ib} > K_{Ic} \tag{5}$$

where K_I, K_{Ib}, and K_{Ic} are stress intensity factor, critical branching stress intensity factor and fracture toughness, respectively. In dynamic fracture, branching occurs when $K_I \geq K_{Ib}(> K_{Ic})$. K_{Ib} is an onset point for branching above which branching can proceed.

Unlike the aforementioned dynamic fracture, the crack in the CVD-graphene turned clearly out to propagate at the stress intensity level less than the fracture toughness (K_{Ic}) under the quasi static loading. Furthermore, the crack propagation

speed in the CVD-graphene (~10^{-2} m/s, see Table S4) was measured to be incomparably far less than the Rayleigh wave speed (V_R = ~158 m/s for homogeneous elastic media), while the crack speed in dynamic fracture can be even faster than V_R [61,62]. In other words, the CVD-graphene showed subcritical crack growth behavior. Up to now, innumerable experimental works have reported that main factors leading to subcritical crack growth are fatigue, stress corrosion and creep [63]. Considering the experimental evidences in literature, the most probable factor which can justify the subcritical crack growth behavior of the CVD-graphene is stress corrosion. The crack subcritically growing in the inhomogeneous materials can easily bifurcate (crack branching) and meander (crack curving) due to the crack deflection at particles or interfaces [64]. More specifically, as many researchers have already reported, interaction of cracks with certain obstacles is frequently observed behavior in most of materials. The deceleration or arrest of crack upon encountering a microstructural barrier or obstacle, such as grain boundary, twin boundary and hard particles is common observation [65,66]. The branching/arresting/curving are general behaviors of subcritically growing crack in an inhomogeneous media.

6. Supplementary Discussion IV

For calculating the stress intensity factor, firstly, the deformed graphene membrane under uniform pressure ($\Delta P \approx 1.5$ kPa) was assumed to be a continuum membrane with an atomistic thickness (Figure S17). It has been long recognized that the fracture behavior of the general materials strongly depends on the tested sample thickness. In other words, a membrane structure with an insignificant thickness can be approximated by plane stress state with the assumption of negligible normal stress in the direction of thickness, while a structure with a significant thickness can be approximated by plane strain state with the assumption of negligible normal strain in the direction of thickness. As a result, it has been considered that the measurement leads to plane stress fracture toughness, K_c, for thin specimen, and plane strain fracture toughness, K_{Ic}, for thick specimen, respectively. The linear transitional relationship between K_c and K_{Ic} has been provided by Anderson [67], subsequently some simplifying hypothesis with respect to the characteristic size of

the plastic zone has led to the approximate relation, $\frac{K_c}{K_{Ic}} = \sqrt{1 + \frac{E}{12} \frac{\varepsilon_f}{\sigma_Y}}$ (ε_f and σ_Y are

fracture strain and yield stress, respectively) [68]. This relation implies that for ideal

brittle material there is no transition due to the absence of yielding, i.e. $K_c \approx K_{Ic}$.

Consequently, given that the graphene reveals nonlinear elastic behavior with

negligible plastic deformation before failure [69], it was readily able to be assumed

as $K_c \approx K_{Ic}$. Based on this fact, later we compared the measured fracture toughness,

K_{Ic} , of the CVD-graphene with the K_{Ic} of other bulk materials mostly measured in

plane strain condition.

The deflection (h) of the graphene membrane was calculated from the continuum

based analytical expression [70], $\Delta P = \frac{2Et}{(1-v)r^4} h^3 + \frac{4\sigma_0 t}{r^2} h$, where, E is the Young's

modulus ($\approx$ 1 TPa [69]), v is the Poisson's ratio (assumed as 0.165, the value for the

graphite in the basal plane [69,71]), t is the graphene thickness ($\approx$ 3.35 Å [72]), r is

the radius of the membrane ($\approx$ 45 µm), σ_0 is the residual tension or pretension

(assumed as zero, the detailed discussion will be followed later), respectively. The

applied quasistatic nominal radial stress (σ) was calculated to be 1.15 GPa from the

expression [70], $\sigma = \frac{\Delta p r^2}{4th}$, and the calculated deflection (h=1.97 µm). The SIF was

calculated from the Irwin's formula [73], $\sigma_{ij} = \frac{K_I}{\sqrt{2\pi r}} f_{ij}(\theta)$, or $K_I = Y\sigma\sqrt{\pi a}$, where Y

is a configuration factor. As the dimensionless Y nonlinearly varies with the

geometry of the specimen the crack is in and the crack length, the precise Y was

hardly determinable. When the crack length is much less than the size of graphene

membrane, Y is obviously equal to 1. However, referring to the report by Erdogan *et

al.*[74] who investigated on the configuration factor of the spherical shell with cracks,

it was able to be confirmed that the Y is likely larger than 1. Although Y can

randomly deviate from 1 as the crack in the graphene membrane grows, here, the Y

was assumed to be 1 for simplicity of analysis (Figure S10) [75]. Because the crack

observed on the CVD-graphene was a slanted crack in a thin infinite membrane

under biaxial loading, mode-**I** fracture as well as mode-**II** fracture were had to be

considered,   i.e. $K_I = \sigma\sqrt{\pi a}(cos\beta^2 + \alpha sin\beta^2)$, $K_{II} = \sigma\sqrt{\pi a}(1 - \alpha)cos\beta sin\beta$,

where $\sigma_x/\sigma_y = \alpha$, β is an angle made by the crack with x-axis (see the schematic

drawing in Figure S17)), respectively. Given that the graphene is under equibiaxial tension, i.e. α=1, the formula was again able to be reduced to $K_I = \sigma\sqrt{\pi a}$. As another agenda, the crack branching was taken into account. In other words, the SIFs of the mother crack $(K_{I,a1})$ and the branched crack$(K_{I,a2})$ were assessed from $K_{I,a1} = \sigma\sqrt{\pi a1}$, and $K_{I,a2} = f(a2/a1)\sigma\sqrt{\pi a2}$, respectively. The value $f(a2/a1)$ was assumed to be 1 on reference to the numerical analysis results [76]. From these approaches, the $K_{I,a1}$ and $K_{I,a2}$ were calculated and the resulting diagrams of $(V_{a1} - K_{I,a1})$ and $(V_{a2} - K_{I,a2})$ were obtained, as shown in Figure 3.

7. Supplementary 4 Movies

Movie S1

High speed video showing fracture behavior of the CVD graphene under room condition.

Movie S2

High speed video showing fracture behavior of the CVD graphene under controlled condition I.

Movie S3

High speed video showing fracture behavior of the CVD graphene under controlled condition II.

Movie S4

High speed video showing fracture behavior of the CVD graphene under controlled condition III.

8. Supplementary References

1.   Li, X. *et al.* Large-area synthesis of high-quality and uniform graphene films on copper foils. *Science* **324**, 1312-1314 (2009).

2.   Suk, J. W. *et al.* Transfer of CVD-grown monolayer graphene onto arbitrary substrates. *ACS Nano* **5**, 6916-6924 (2011).

3. Wiederhorn, S. M., Freiman, S. W., Fuller Jr, E. R. & Simmons, C. J. Effects of water and other dielectrics on crack growth. *J. Mater. Sci.* **17**, 3460-3478 (1982).

4. Charles, R. J. Static fatigue of glass. I. *J. Appl. Phys.* **29**, 1549-1553 (1958).

5. Charles, R. J. Static fatigue of glass. II. *J. Appl. Phys.* **29**, 1554-1560 (1958).

6. Atkinson, B. K. Subcritical crack growth in geological materials. *J. Geophys. Res.* **89**, 4077-4114 (1984).

7. Wiederhorn, S. M. Influence of water vapor on crack propagation in soda-lime glass. *J. Am. Ceram. Soc.* **50**, 407-414 (1967).

8. Bhargava, A. K. *Engineering Materials: Polymers Ceramics And Composites* (PHI Learning Pvt. Ltd., 2005).

9. Ashby, M. F. & Jones, D. R. H. *Engineering materials: an introduction to their properties and applications* (Pergammon, 1980).

10. Ashby, M. F. *Materials selection in mechanical design* (Elsevier, 2005).

11. Field, J. E. & Freeman, C. J. Strength and fracture properties of diamond. *Phil. Mag.* **43**, 595-618 (1981).

12. Drory, M. D., Dauskardt, R. H., Kant, A. & Ritchie, R. O. Fracture of synthetic diamond. *J. Appl. Phys.* **78**, 3083-3088 (1995).

13. Hodkinson, P. H. & Nadeau, J. S. Slow crack growth in graphite. *J. Mater. Sci.* **10**, 846-856 (1975).

14. Omeltchenko, A., Yu, J., Kalia, R. K. & Vashishta, P. Crack front propagation and fracture in a graphite sheet: a molecular-dynamics study on parallel computers. *Phys. Rev. Lett.* **78**, 2148-2151 (1997).

15. Xu, M., Tabarraei, A., Paci, J. T., Oswald, J. & Belytschko, T. A coupled quantum/continuum mechanics study of graphene fracture. *Int. J. Fract.* **173**, 163-173 (2012).

16. Becher, P. F. Subcritical crack growth in partially stabilized ZrO_2(MgO). *J. Mater. Sci.* **21**, 297-300 (1986).

17. Suratwala, T. I. & Steele, R. A. Anomalous temperature dependence of sub-critical crack growth in silica glass. *J. Non-Cryst. Solids* **316**, 174-182 (2003).

18. Ebrahimi, M. E., Chevalier, J. & Fantozzi, G. Slow crack-growth behavior of alumina ceramics. *J. Mater. Res.* **15**, 142-147 (2000).

19. Chevalier, J., De Aza, A. H., Fantozzi, G., Schehl, M. & Torrecillas, R. Extending the lifetime of ceramic orthopaedic implants. *Adv. Mater.* **12**, 1619-1621 (2000).

20. De Aza, A. H., Chevalier, J. & Fantozzi, G. Slow-crack-growth behavior of zirconia-toughened alumina ceramics processed by different methods. *J. Am. Ceram. Soc.* **86**, 115-120 (2003).

21. Wang, Y. Y. *et al.* Raman studies of monolayer graphene: the substrate effect. *J. Phys. Chem. C* **112**, 10637-10640 (2008).

22. Lazzeri, M. & Mauri, F. Nonadiabatic Kohn anomaly in a doped graphene monolayer. *Phys. Rev. Lett.* **97**, 266407 (2006).

23. Ando, T. Anomaly of optical phonon in monolayer graphene. *J. Phys. Soc. Jpn.* **75**, 124701 (2006).

24. Yan, J., Zhang, Y. B., Kim, P. & Pinczuk, A. Electric field effect tuning of electron-phonon coupling in graphene. *Phys. Rev. Lett.* **98**, 166802 (2007).

25. Pisana, S. *et al.* Breakdown of the adiabatic Born–Oppenheimer approximation in graphene. *Nature Mater.* **6**, 198-201 (2007).

26. Yan, J., Zhang, Y., Kim, P. & Pinczuk, A. Electric field effect tuning of electron-phonon coupling in graphene. *Phy. Rev. Lett.* **98**, 166802 (2007).

27. Ni, Z. H. *et al.* Probing charged impurities in suspended graphene using Raman spectroscopy. *ACS Nano* **3**, 569-574 (2009).

28. Das, A. *et al.* Monitoring dopants by raman scattering in an electrochemically top-gated graphene transistor. *Nat. Nanotechnol.* **3**, 210-215 (2008).

29. Casiraghi, C., Pisana, S., Novoselov, K. S., Geim, A. K. & Ferrari, A. C. Raman fingerprint of charged impurities in graphene. *Appl. Phys. Lett.* **91**, 233108 (2007).

30. Kalbac, M. *et al.* The influence of strong electron and hole doping on the raman intensity of chemical vapor-deposition graphene. *ACS Nano* **4**, 6055-6063 (2010).

31. Dong, X. *et al.* Doing single-layer graphene with aromatic molecules. *Small* **5**, 1422-1426 (2009).

32. Schedin, F. *et al.* Detection of individual gas molecules adsorbed on graphene. *Nature Mater.* **6**, 652-655 (2007).

33. Das, B., Voggu, R., Rout, C. S. & Rao, C. N. R. Changes in the electronic structure and properties of graphene induced by molecular charge-transfer. *Chem. Commun.* 5155-5157 (2008).

34. Bonini, N., Lazzeri, M., Marzari, N. & Mauri, F. Phonon anharmonicities in graphite and graphene. *Phys. Rev. Lett.* **99**, 176802 (2007).

35. Balandin, A. A. *et al.* Superior thermal conductivity of single-layer graphene. *Nano Lett.* **8**, 902-907 (2008).

36. Cai, W. W. *et al.* Thermal transport in suspended and supported monolayer graphene grown by chemical vapor deposition. *Nano Lett.* **10**, 1645-1651 (2010).

37. Chen, S. *et al.* Raman measurements of thermal transport in suspended monolayer graphene of variable sizes in vacuum and gaseous environments. *ACS Nano* 5, 321-328 (2011).

38. Mohiuddin, T. M. G. *et al.* Uniaxial strain in graphene by Raman spectroscopy: G peak splitting, Grüneisen parameters, and sample orientation. *Phys. Rev. B* **79**, 205433 (2009).

39. Metzger, C. *et al.* Biaxial strain in graphene adhered to shallow depressions. *Nano Lett.* **10**, 6-10 (2010).

40. Ding, F. *et al.* Stretchable graphene: a close look at fundamental parameters through biaxial straining. *Nano Lett.* **10**, 3453-3458 (2010).

41. Zabel, J. *et al.* Raman spectroscopy of graphene and bilayer under biaxial strain: bubbles and balloons. *Nano Lett.* **12**, 617-621 (2012).

42. Chen, C.-C. *et al.* Raman spectroscopy of ripple formation in suspended graphene. *Nano Lett.* **9**, 4172-4176 (2009).

43. Shivaraman, S. *et al.* Free-standing epitaxial graphene. *Nano Lett.* **9**, 3100-3105 (2009).

44. Zabel, J. *et al.* Raman spectroscopy of graphene and bilayer under biaxial strain: bubbles and balloons. *Nano Lett.* **12**, 617-621 (2012).

45. Pan, W. *et al.* Biaxial compressive strain engineering in graphene/boron nitride heterostructures. *Sci. Rep.* **2**, 893 (2012).

46. Yoon, D., Son, Y.-W. & Cheong, H. Negative thermal expansion coefficient of graphene measured by Raman spectroscopy. *Nano Lett.* **11**, 3227-3231 (2011).

47. Shi, Y., Dong, X., Chen, P., Wang, J. & Li, L.-J. Effective doping of single-layer graphene from underlying SiO_2 substrates. *Phys. Rev. B* **79**, 115402 (2009).

48. Kang, Y.-J., Kang, J. & Chang, K. J. Electronic structure of graphene and doping effect on SiO_2. *Phys. Rev. B* **78**, 115404 (2008).

49. Nistor, R. A., Kuroda, M. A., Maarouf, A. A. & Martyna, G. J. Doping of adsorbed graphene from defects and impurities in SiO_2 substrates. *Phys. Rev. B* **86**, 041409 (2012).

50. Lee, J. E., Ahn, G., Shim, J. Lee, Y. S. & Ryu, S. Optical separation of mechanical strain from charge doping in graphene. *Nat. Commun.* **3**, 1024 (2012).

51. Duong, D. L. *et al.* Probing graphene grain boundaries with optical microscopy. *Nature* **490**, 235-239 (2012).

52. Kim, K. *et al.* Ripping graphene: preferred directions. *Nano Lett.* **12**, 293-297 (2012).

53. Fineberg, J., Gross, S. P., Marder, M. & Swinney, H. L. Instability in dynamic fracture. *Phys. Rev. Lett.* **67**, 457-460 (1991).

54. Sharon, E., Gross, S. P. & Fineberg, J. Local crack branching as a mechanism for instability in dynamic fracture. *Phy. Rev. Lett.* **74**, 5096-5099 (1995).

55. Xu, L. R. & Rosakis, A. J. Real-time experimental investigation of dynamic crack branching using high-speed optical diagnostics. *Exp. Techniques* **27**, 23-26 (2003).

56. Kobayashi, A. S. & Mall, S. Dynamic fracture toughness of Homalite-100. *Exp. Mech.* **18**, 11-18 (1978).

57. Ramulu, M., Kobayashi, A. S. & Kang, B. S.-J. Dynamic crack curving and branching in line-pipe. *J. Pressure Vessel Technol.* **104**, 317-322 (1982).

58. Ramulu, M. & Kobayashi, A. S. Mechanics of crack curving and branching-a dynamic fracture analysis. *Int. J. Fract.* **27**, 187-201 (1985).

59. Kobayashi, A. S., Ramulu, M., Dadkhah, M. S., Yang, K. -H. & Kang, B. S.-J. Dynamic fracture toughness. *Int. J. Fract.* **30**, 275-28 (1986).

60. Rabinovitch, A. & Bahat, D. Differentiation of crack branching types in fractured glass. *Europhys. Lett.* **95**, 16003 (2011).

61. Rosakis, A. J., Samudrala, O. & Coker, D. Cracks faster than the shear wave speed. *Science* **284**, 1337-1340 (1999).

62. Abraham, F. F. & Gao, H. How fast can cracks propagate?. *Phys. Rev. Lett.* **84**, 3113-3116 (2000).

63. Miller, K. J. *Subcritical Crack Growth due to Fatigue, Stress Corrosion and Creep* (ed. L. H. Larsson, Elsevier Applied Science, London, 1984).

64. Ritchie, R. O. Mechanisms of fatigue-crack propagation in ductile and brittle solids. *Int. J. Fract.* **100**, 55-83 (1999).

65. Miller, K. J. Metal fatigue-past, current and future. *Proc. Instn. Mech. Engrs.* **205**, 291-304 (1991).

66. Wang, C. H. & Hutchinson, J. W. Interactions of fatigue cracks with elastics obstacles. *Int. J. Fract.* **109**, 263-283 (2001).

67. Anderson, W. E. *Some designer-oriented views on brittle fracture.* Battle northwest report BNLW-SA-2290 (1960).

68. Broek, D. *Elementary Engineering Fracture Mechanics.* 4th edn, (Martinus Nijhoff Publishers, 1986).

69. Lee, C., Wei, X., Kysar, J. W. & Hone, J. Measurement of the elastic properties and intrinsic strength of monolayer graphene. *Science* **321**, 385-388 (2008).

70. Xu, D. & Liechti, K. M. Bulge testing transparent thin films with Moiré deflectometry. *Exp. Mech.* **50**, 217-225 (2010).

71. Blakslee, O. L., Procor, D. G., Seldin, E. J., Spence, G. B. & Weng, T. Elasitic constants of compression-annealed pyrolytic graphite. *J. Appl. Phys.* **41**, 3373-3382 (1970).

72. Al-Jishi, R. & Dresselhaus, G. Lattice-dynamical model for graphite. *Phys. Rev. B* **26**, 4514-4522 (1982).

73. Irwin, G. R. Analysis of stresses and strains near the end of a crack traversing a plate. *J. Appl. Mech.* **24**, 361-364 (1957).

74. Erdogan, F. & Kibler, J. J. Cylindrical and spherical shells with cracks. *Int. J. Frac. Mech.* **5**, 229-237 (1969).

75. Xiang, Y., McKinnell, J., Ang, W.-M. & Vlassak, J. J. Measuring the fracture toughness of ultra-thin films with application to AlTa coatings. *Int. J. Fract.* **144**, 173-179 (2007).

76. Daux, C., Moës, N., Dolbow, J., Sukumar, N. & Belytschko, T. Arbitrary branched and intersecting cracks with the extended finite element method. *Int. J. Numer. Mech. Engng.* **48**, 1741-1760 (2000).

77. Goossens, A. M. *et al.* Mechanical cleaning of graphene. *Appl. Phys. Lett.* **100**, 073110 (2012).

78. Lindvall, N., Kalabukhov, A. & Yurgens, A. Cleaning graphene using atomic force microscope. *J. Appl. Phys.* **111**, 064904 (2012).